An experimental study to characterize the effects of initial ice roughness on the wind-driven water runback over an airfoil surface

Yang Liu [a,b], Kai Zhang [a], Wei Tian [a,c], Hui Hu [a,c,*]

[a] Department of Aerospace Engineering, Iowa State University, Ames, IA 50011, USA.
[b] Department of Engineering, East Carolina University, Greenville, NC 27858, USA
[c] School of Aeronuatics and Astronaustics, Shanghai JiaoTong University, Shanghai, China

A R T I C L E   I N F O

A B S T R A C T

In the present study, an experimental study was conducted to characterize the effects of initial ice roughness on the transient behaviors of surface water/ice run-back over a NACA 23012 airfoil model under a glaze icing condition. The experimental study was conducted in the Icing Research Tunnel of Iowa State University (i.e., ISU-IRT). A digital image projection (DIP) technique was applied to provide non-intrusive, temporally-and-spatially-resolved measurements of the thickness distributions of the dynamic water/ice flows over the airfoil surface. Two typical surface morphologies were observed for the surface water runback over the airfoil models: water film flow and water rivulets flow. While the surface water film flow modulated with one primary wave and multiple secondary waves is observed at lower wind speed conditions (i.e., $U_\infty = 10$ m/s), the water rivulets flow is observed at relatively higher wind speed conditions (i.e., $U_\infty = 15$ m/s). The initial ice roughness is found to retard and shorten the primary wave formation in the water film flow. It is also found that the initial ice roughness could trap and decelerate the water flow and decrease the inertia force in the film front, which essentially delays the formation of the rivulets. The water rivulet flow trapped by the initial roughness was found to have a meandering behavior, due to which, the initially formed narrow rivulets merged into wider rivulets as they move downstream. By recognizing the film/rivulets boundary during the dynamic surface water/ice runback process, the quantitative details were extracted, i.e., the formation, transition, and development of the rivulet flows. The initial ice roughness was found to have a significant effect on the rivulet characteristics (e.g., rivulet width, spacing, and height).

© 2020 Elsevier Ltd. All rights reserved.

1. Introduction

Aircraft icing is widely recognized as one of the most serious threats to flight safety (Potapczuk, 2013). Aircraft performance can be severely contaminated due to ice accretion, which can cause stall margin reduction, drag increase, and lift decrease (Gent et al., 2000). It is documented that more than 1100 icing-related accidents and incidents occurred in the US from 1978 to 2010 (Appiah-Kubi, 2011; Green, 2006; Petty and Floyd, 2004). The in-flight ice formation and morphology are generally determined by icing cloud conditions (e.g., liquid water content (LWC), air temperature, and droplet size). As aircraft operate in the cloud with low LWC, small droplets, and cold temperatures (typically below −10 °C), the droplets freeze immediately upon impact on the aircraft surface. Rime ice with rough, milky white appearance tends

to form conforming to the aerodynamic shapes of aircraft. While under other cloud conditions with high LWC, large droplets, and temperature just below the freezing point, the impinged water runs back over aircraft surface before freezing downstream. Glaze ice forms with smooth, dense, and transparent appearance, and deforms into horn-like shapes as more water is transported and freezes (Hansman and Kirby, 1987). These ice shapes extend into the airflow, and therefore, affect the aerodynamic and heat transfer characteristics. Glaze ice has been considered as the most dangerous icing hazard (Gent et al., 2000).

Accurate modeling and prediction of ice accretion could aid in the design of ice protection systems to mitigate icing effect and improve the determination of safety operating conditions (Tecson and McClain, 2013a). However, the current icing simulation programs are limited in their capabilities to accurately predict glaze ice accretion, partly due to the use of simplified ice roughness models. In the LEWICE program, for example, ice roughness height is estimated based on the sand-grain equivalent model. As compared with the ice shapes produced in the icing experiments,

the predicted ice shapes do not match well with the experimental results (Shin, 1996; Vargas, 2007). The initial roughness is suggested to be a key factor affecting icing process (Dukhan et al., 1996; Henry et al., 1994, 2000; Yamaguchi and Hansman, 1992).

A number of experimental studies have been conducted to evaluate the effects of simulated regular roughness (Bragg et al., 1996; Henry et al., 1995; Kerho and Bragg, 1995; Winkler and Bragg, 1996). While regular roughness is easy to implement, they may not properly reflect the irregularity and broad range of topographical scales of practical roughness (Bons and Christensen, 2007). Different ice accretions have unique surface features that are not well captured by ordered arrays of discrete roughness elements. The use of regular roughness would create biases compared with that using realistic roughness (Bons, 2002; Mart et al., 2012). To better understand the effects of the actual ice roughness, various methods have been developed to create realistic ice roughness distributions (Rothmayer, 2003; Tecson and McClain, 2013b). Lagrangian droplet simulator is one of the recent techniques that can generate roughness distributions with bead elements in random distribution and diameters (Tecson and McClain, 2013b, 2013a). However, this method only operates with uniform droplet diameter, which differs from actual icing conditions. In recent years, laser-based and other optical scanning methods have been developed to accomplish three-dimension digitization of ice accretions (Lee et al., 2012). Recently developed 3-D laser scanners have been applied in generating 3-D point cloud containing details of ice roughness and shapes (Lee et al., 2014). A NACA 23012 airfoil with realistic ice roughness has been successfully recreated based on the 3-D scanning method (Liu et al., 2020). The effect of the realistic roughness on the transient ice accretion and heat transfer process has been experimentally studied (Liu et al., 2020). However, the microphysical details in water run-back process associated with glaze icing are still unknown, which is suggested to be of great importance in determining the morphology and growth of glaze ice (Du et al., 2010).

To quantify the microphysical details in water/ice transport process and evaluate the interaction between the initial ice roughness and surface water transport, advanced experimental techniques capable of providing accurate quantitative measurements of surface morphology are highly desired. In recent years, various measurement techniques have been developed to achieve quantitative, non-intrusive measurements of thickness distribution/surface morphologies of different substances (Benetazzo, 2006; Liu et al., 2017, 2016a, 2016b; Zhang et al., 2015; Zhang et al., 2014), among which the structured light technique has been successfully applied in reconstructing various surfaces. The basic methodology of this technique is to actively project known light patterns onto a surface, and extracting 3-D surface shapes from the images of the light patterns captured from one or more points of view. In recent years, this technique has been introduced to measure fluid flow (Cazabat et al., 1990; Cobelli et al., 2009; Hu et al., 2014; Zhang and Su, 2002). For example, a novel digital image projection (DIP) technique developed by Zhang et al. (2015) has been demonstrated to be a very reliable measurement tool to reconstruct the complex three-dimensional (3D) surface features of a water film/rivulets flow over an airfoil surface. The microphysical details from droplet impingement to water film/rivulets formation and runback were revealed based on the DIP measurements. In the present study, the same DIP technique was implemented to provide non-intrusive, temporally resolved, and full-field measurements of the dynamic water/ice thickness distributions over the surface of an NACA 23,012 airfoil. Based on the quantitative DIP measurements, evolutions of the surface water/ice film and rivulet features generated at the air/water interface were revealed clearly and quantitatively in both time and space scales.
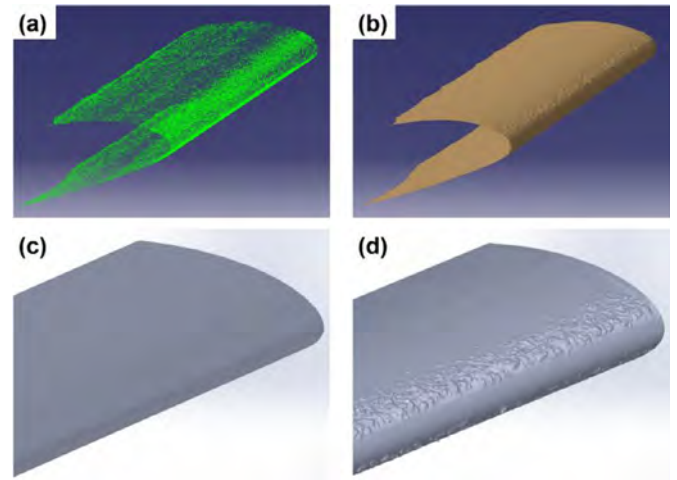

Fig. 1. (a) Point cloud of a 3D scanned NACA 23012 airfoil with ice roughness; (b) Rendered airfoil surface with ice roughness features; (c) Airfoil model with smooth leading edge; (d) Airfoil model with rough leading edge.

2. Experimental methodology

2.1. Airfoil model with initial ice roughness

The test model used in the present study is an NACA 23012 airfoil with realistic initial ice roughness. The initial ice roughness was formed under a typical in-flight icing condition (i.e., wind speed of U_∞=102.9 m/s; LWC=0.75 g/m³; MVD = 15 μm, and airflow temperature of T_∞ =−2.2 °C, with a icing duration of 30 s) in the Icing Research Tunnel (IRT) at NASA's Glenn Research Center (Lee et al., 2012). The iced airfoil model was then 3-D scaned using a Romer Absolute Arm System. It should be noted that, due to the transparent nature of ice, spray painting was usually used to achieve valid 3-D scanning operations. As decribed in Lee et al. (2012), this may introduce additional errors for the ice roughness measurements. The point cloud data file generated in the 3-D scan was used as the input file for rebuilding the solid airfoil model with realistic ice roughness. The construction of the solid airfoil model from the point cloud data is a typical reverse engineering project. The point cloud file was imported into a 3D CAD software (CATIA-V5-R20 in this study) as shown in Fig. 1(a). The imported point cloud was then manipulated (i.e., points filter, local and global points activate and remove) to generate a mesh surface containing the ice roughness features as can be seen in Fig. 1(b). The mesh surface was further treated by filling holes, flipping edges, and cleaning non-manifold meshes to create the airfoil surface with realistic ice roughness. Finally, the faces and solid body were generated by using the Quick Surface Reconstruction (QSR) module in the CAD software. The airfoil models with smooth and rough leading edges (i.e., SLE and RLE) were finished and 3-D printed as shown in Fig. 1(c) and (d). It can be clearly seen that, while the roughness elements are of various shapes and sizes and randomly distributed, the stagnation region appears to be smooth which is consistent with the previous studies (Hansman et al., 1991).

By comparing the ice roughened airfoil model and the original smooth airfoil model, the root-mean-square roughness height for the rough surface can be calculated following the work by McClain et al. (McClain et al., 2017; McClain and Kreeger, 2013; Tecson and McClain, 2013b):

$$R_q = \left[\frac{1}{N} \sum_{i=1}^{N} (y_i - \bar{y}_i)^2 \right]^{\frac{1}{2}} \tag{1}$$
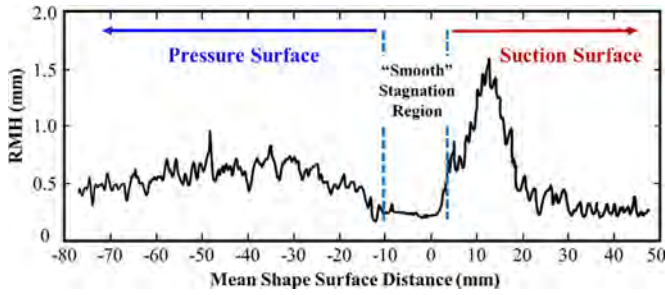
Fig. 2. Roughness distribution over the NACA 23012 airfoil model.

where N is the number of points at a specific surface distance, $(y_i - \bar{y}_i)$ is the local height difference between the ice-roughened surface and the smooth surface. Thus, the 99% roughness maximum height (RMH) based on a Gaussian distribution can be calculated using three times the root-mean-square roughness height (McClain and Kreeger, 2013):

$$RMH = 3R_q = 3\left[\frac{1}{N}\sum_{i=1}^{N}(y_i - \bar{y}_i)^2\right]^{\frac{1}{2}} \tag{2}$$

Fig. 2 shows the ice roughness distribution over the airfoil model. It should be noted that the roughness distribution agrees well with that extracted using a Self-Organizing-Map approach by McClain (McClain and Kreeger, 2013). As can be seen clearly in Fig. 2, there is a significant difference between the roughness height on the suction side and that on the pressure side of the airfoil model, as separated by the "smooth" stagnation region. It is suggested that such difference is essentially caused by the asymmetrical profile of the NACA 23012 airfoil, which influences the water collection efficiency and heat transfer properties. In the present study, only two model configurations (i.e., airfoil model with smooth leading edge vs. airfoil model with initial ice roughness around leading edge) were used to provide a comparative study to reveal the effects of initial realistic ice roughness on the surface water/ice behaviors during dynamic icing process.

2.2. Icing research tunnel used in the present study

In the present study, the experiments were carried out in the unique Icing Research Tunnel available at Aerospace Engineering Department of Iowa State University (i.e., ISU-IRT). ISU-IRT is a multifunctional icing research tunnel with a test section of 2.0 m in length × 0.4 m in width × 0.4 m in height with four sidewalls being optically transparent. It has a capacity of generating a maximum wind speed of 60 m/s and an airflow temperature down to −25 °C. An array of 8 pneumatic atomizer/spray nozzles are installed at the entrance of the contraction section of the icing tunnel to inject micro-sized water droplets (10 ~ 100 μm in size with MVD $\approx$ 20 μm) into the airflow. By manipulating the water flow rate through the spray nozzles, the liquid water content (LWC) in the ISU-IRT could be adjusted (i.e., *LWC* ranging from 0.1 g/m^3 to 5.0 g/m^3). In summary, ISU-IRT can be used to simulate atmospheric icing phenomena over a range of icing conditions (i.e., from dry *rime* to extremely wet *glaze* ice conditions) (Liu and Hu, 2018; Waldman and Hu, 2015).

The test airfoil models (i.e., NACA 23012 airfoil with and without the initial leading-edge roughness) were made of a hard-plastic material and manufactured by using a rapid prototyping machine (i.e., 3-D printing) that builds 3-D models layer-by-layer with a resolution of about 25 μm. Supported by a stainless-steel rod, the airfoil model was mounted at its quarter-chord and oriented horizontally across the middle of the test section. In the present study,
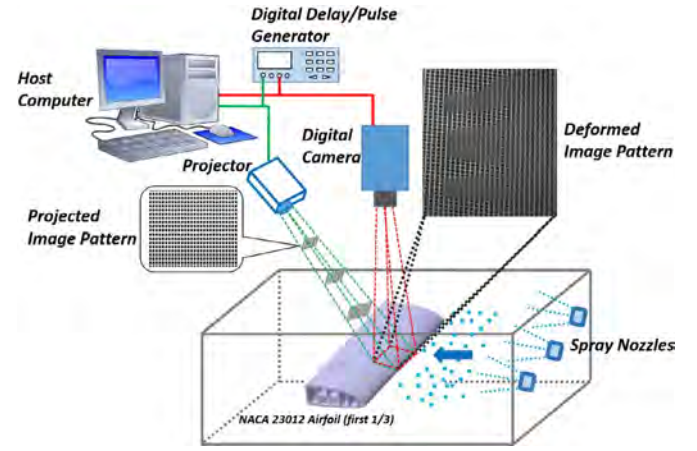

Fig. 3. Schematic of experimental setup for the digital image projection (DIP) technique.

to reproduce the water run-back phenomena in glaze icing, while the LWC was set to LWC = 5.0 g/m^3 and the airflow temperature was set at $T_\infty = -5$ °C, the incoming airflow velocity was set at $U_\infty = 10 ~ 15$ m/s to generate different surface water runback behaviors. Multiple runs (i.e., at least three runs) were conducted for each test case. It should be noted that, while slight variations of the water/ice thickness and rivulets width were observed due to the unsteady/nonlinear nature of the ice accretion process, the global features and general characteristics of the surface water/ice morphology were found to be rather similar in the different test runs of the same test case, owing to the well-controlled icing test conditions, i.e., LWC level, wind speed, temperature, and droplet size, in the ISU-IRT.

2.3. Digital image projection technique

The digital image projection (DIP) technique has been reported in great details in the previous study by Zhang et al. (2015). In a typical DIP system, while a digital projector is used to project image patterns with specific characteristics onto an object surface, a digital camera is used to record the distorted image patterns from a different perspective. In the present study, the DIP technique was applied to quantify the transient water/ice runback process over the airfoil models with and without the leading-edge roughness.

The schematic of the experimental setup for the DIP technique is shown in Fig. 3. A digital projector (DLP® LightCrafter™) was used to project the grid-patterned image as shown in the figure. A high-speed camera (PCO Tech, Dimax) with a 60 mm lens (Nikon, 60 mm Nikkor f/2.8) was mounted above the test section. The camera was positioned normal to the airfoil chord, providing a field of view of 1280 × 1024 pixels^2. As water film/rivulets appear on the airfoil surface, the grid pattern deforms; and the deformed pattern can be captured by the camera as can be seen in Fig. 3. The digital camera and the projector were synchronized with a digital delay/pulse generator (BNC Model 575–8C). In the present study, the frame rate for the image acquisition was set to 50 Hz to resolve the transient details of the surface water/ice run-back behavior over the airfoil models.

It has been derived in the previous study that the pixel displacement in a deformed image pattern is linearly related to the local height change at the corresponding point of interest (Zhang et al., 2015). By performing a calibration procedure similar as that described in the previous work (Hu et al., 2014; Zhang et al., 2015), the displacement-to-height conversion map (i.e., "*K*" map) can be obtained. For the calibration in this study, the target plate with grid pattern was moved along the vertical
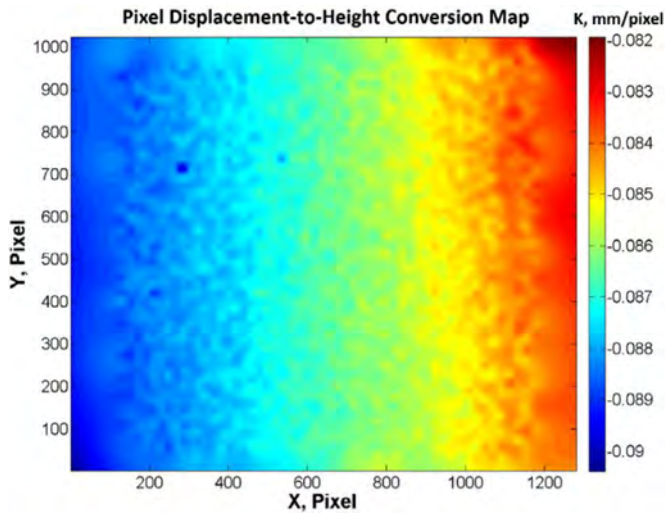
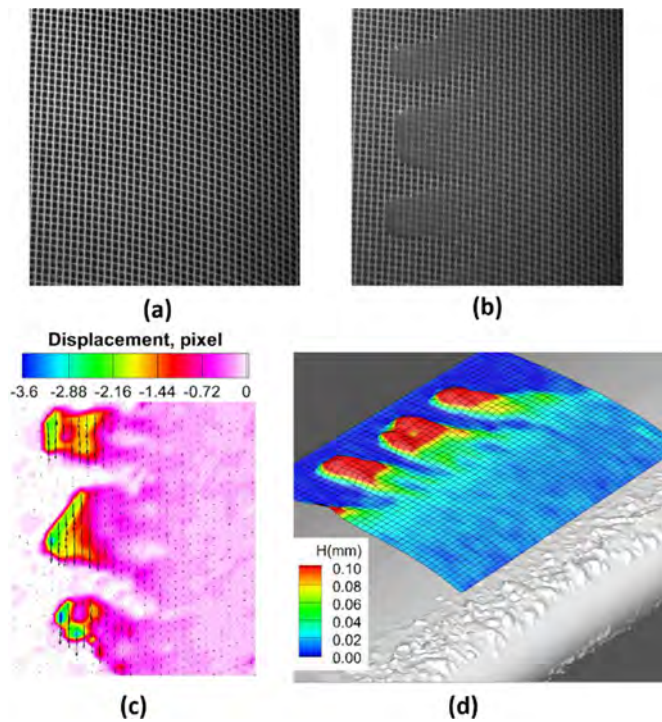**Fig. 4.** The displacement-to-height factor distribution in the measuring field.

Fig. 5. Typical raw images, pixel displacement map, and surface topography obtained in the DIP measurements. (a) Reference image; (b) Deformed image with the presence of water film/rivulet flow; (c) Pixel displacement map; (d) Surface topography of the airfoil model with surface water/ice runback.

direction. Then, the calibration images were collected at 27 parallel positions with an interval of 0.635 mm. The pixel displacement map between each two successive images was derived by performing the cross-correlation algorithm (Zhang et al., 2015). Thus, the displacement-to-height conversion map in the measuring field can be integrated as shown in Fig. 4.

With the displacement-to-height conversion map, the surface water film/rivulets morphology can be reconstructed based on the pixel displacement distribution. Here, the routine operation for a typical raw image pair (including a reference image and a pattern-deformed image as can be seen in Fig. 5(a) and (b)) acquired in the DIP measurements will be described in brief. It can be found that the grid pattern in the reference image is curved as fitting with

the airfoil camber. All of the "Cross" units in the reference image can be detected and saved in a coordinate matrix. As water/ice appears on the airfoil surface, the grid pattern will deform as shown in Fig. 5(b). Then, the coordinate matrix is applied to the deformed image as estimated "Cross" locations. For each estimated location, a cross-correlation algorithm will be applied and looped in a defined searching window around it to find the real "Cross" location. Thus, the displacement of each "Cross" unit can be determined as shown in Fig. 5(c). By multiplying the displacement-to-height conversion factor, the local water/ice thickness can be calculated, and thus, the full-field water/ice thickness distribution can be reconstructed as shown in Fig. 5(d). It can be clearly seen that the film and rivulet shapes are well defined, and the surface morphology conforms well to the pattern-deformed raw image.

The uncertainty of the DIP measurements is mainly determined by the angle between the projector and camera; the distance between projector, camera, and object; and the resolution of the projector and camera (Zhang et al., 2015). As suggested by Gendrich and Koochesfahani (1996), the measurement uncertainty of cross displacement in the correlation process is given by a 95% confidence limit of about ±0.2 pixel, or an rms accuracy of ±0.1 pixel, assuming a Gaussian distribution for error. Considering a maximum displacement of 5 pixels between the distorted images and reference image in the DIP measurements given in the present study, the sub-pixel accuracy in the correlation calculation is about 2.0%.

3. Measurement results and discussions

3.1. Transient water/ice runback processes over the airfoil model with and without initial ice roughness

Fig. 6 shows the time-evolution of the surface water run-back process over the airfoil model with smooth leading edge under the test condition of $U_\infty = 10$ m/s, LWC = 5.0 g/m^3, and $T_\infty = -5$ °C. It is clearly seen that, when water droplets impinged on the airfoil model, since the heat transfer was not adequate to remove all of the latent heat of fusion in the water droplets. Most of the water mas was found to run back as driven by the aerodynamic force (Liu and Hu, 2016). At the very beginning (i.e., $t = t_0 + 0.5$ s), the water droplets deformed and coalesced into beads around the leading edge, a portion of which can be found at the forefront of the measuring window shown in Fig. 6(a). As more water droplets impinged onto the airfoil/wing surface, the water beads ran back and merged into a water film with an evident wave (known as the primary wave) front as can be seen at the image acquired at $t = t_0 + 1.5$ s. The formation of such surface water film indicates that the surface tension, inertia force in the advancing film front and the aerodynamic force acting on it would be in equilibrium (Zhang and Hu, 2016). Sheared by the boundary layer flow, the primary wave moved downstream as the time goes by. In the meantime, more droplets were collected onto the surface and collected into the water film flow. Under the effects of surface tension and aerodynamic force, secondary wave was found to develop and move downstream as can be seen at $t = t_0 + 3.5$ s. As the primary wave moved downstream, the secondary wave advanced over the wetted surface with a higher velocity and finally merged into the primary wave ($t = t_0 + 4.0$ s). Since the water droplets continuously impinged onto the wing surface, there was a periodical secondary wave formation and development ($t = t_0 + 4.0 \sim 9.5$ s). All of the secondary waves were finally merged into the primary wave as it advanced.

While the test condition was kept the same, the surface water film runback behavior was found to be changed over the airfoil model with the initial leading-edge roughness as shown in Fig. 7. It can be seen that the measuring field was set right after the
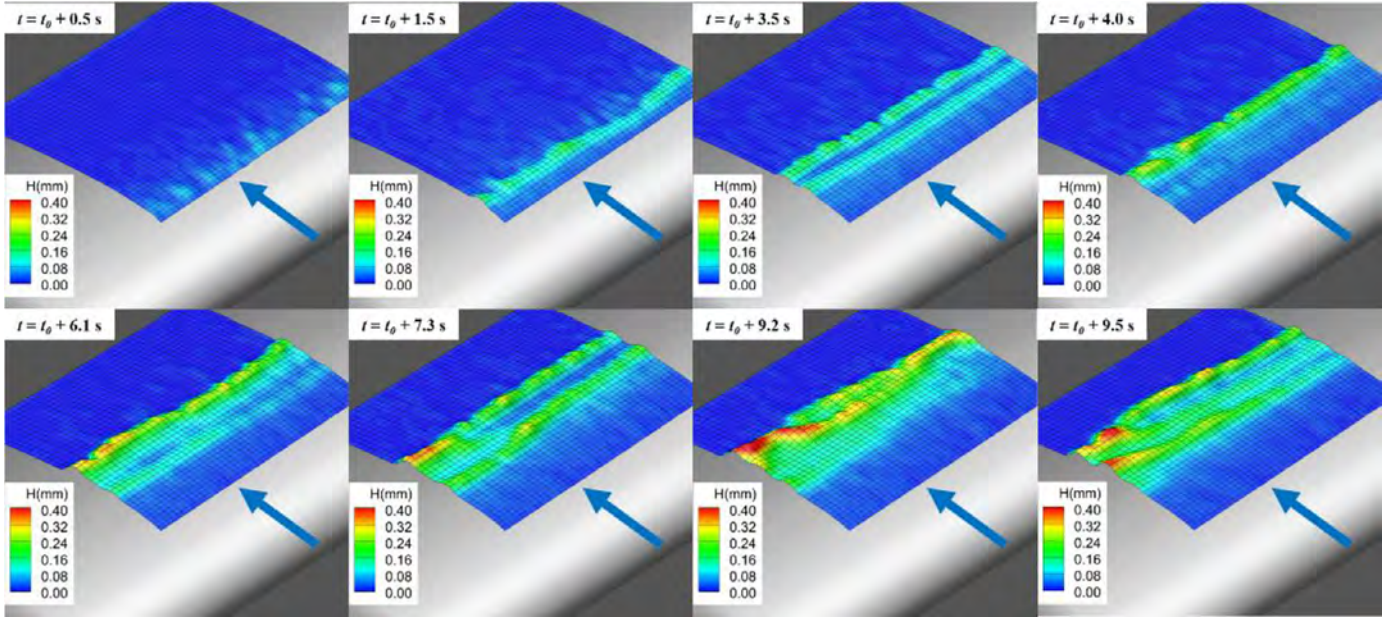
Fig. 6. Time-evolution of the surface water film formation and propagation over the airfoil model with smooth leading edge under the test condition of $U_\infty = 10$ m/s, LWC = 5.0 g/m^3, and $T_\infty = -5$ °C.
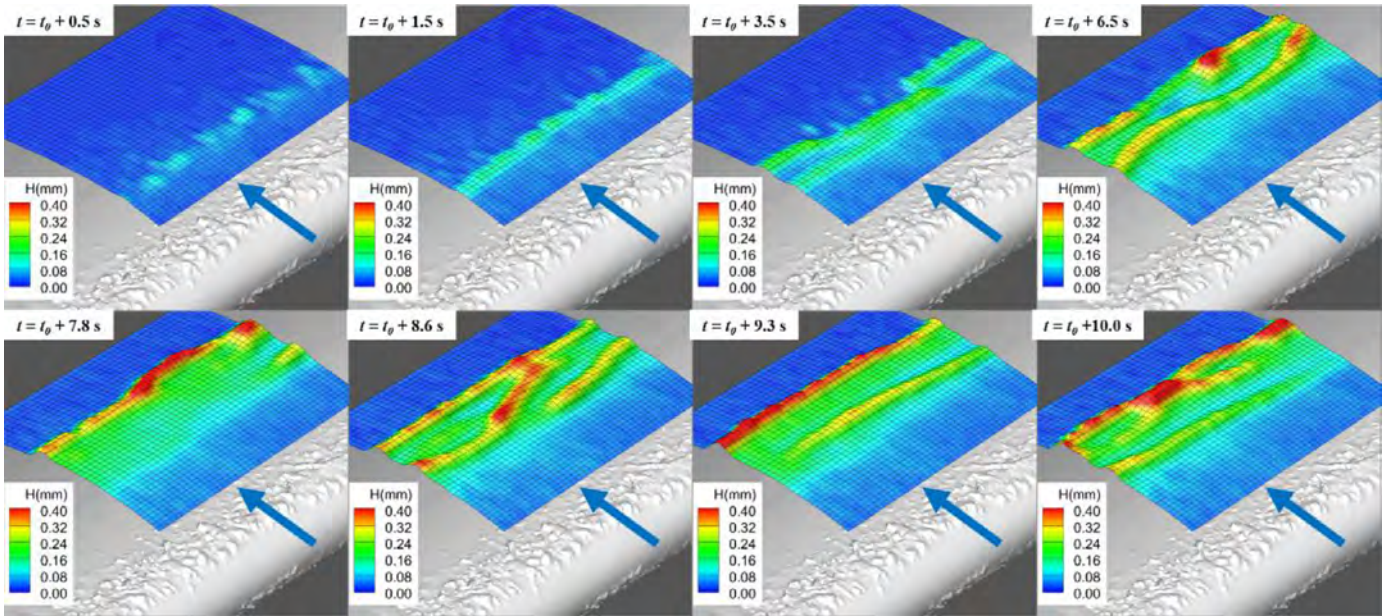

Fig. 7. Time-evolution of the surface water film formation and propagation over the airfoil model with initial leading-edge roughness under the test condition of $U_\infty = 10$ m/s, LWC = 5.0 g/m^3, and $T_\infty = -5$ °C.

roughness. As water droplets impinged onto the wing surface, the initial roughness essentially altered the water collection distribution and transport behavior (Liu and Hu, 2016). It is found that at the early stage ($t = t_0 + 0.5 \sim 1.5$ s), the first water wave (primary wave) front formed as the water droplets ran back and coalesced into a film. However, the location of the wavefront formation was found to start at further downstream in comparison with the case with the smooth airfoil leading-edge. The initial ice roughness is suggested to trap the water runback, which results in the retardation of the wave formation. As time goes by, the primary wave moved downstream, and multiple secondary waves formed and developed as can be seen from $t = t_0 + 3.5$ to 6.5 s. The secondary waves advanced over the wetted surface and finally merged into the primary wave ($t = t_0 + 7.8$ s). With the time

going on, more secondary waves developed downstream and advanced the primary wave ($t = t_0 + 7.8 \sim 10.0$ s).

As wind speed was increased to $U_\infty = 15$ m/s, the runback water appears to be in evident rivulet shapes over the airfoil model with the smooth leading-edge as shown in Fig. 8. It has been demonstrated that the stability of the advancing water film is determined by the surface tension, the inertia force on the film front, and the aerodynamic force at the water/air interface (Zhang and Hu, 2016). As a direct consequence of the wind speed increase, the inertia force and the aerodynamic force will increase while the surface tension remains the same. Thus, the force balance at the advancing film front would break, leading to the formation of the multiple rivulets. It can be seen clearly that, at the very early stage ($t \leq t_0 + 1.0$ s), the impinged water droplets first merged
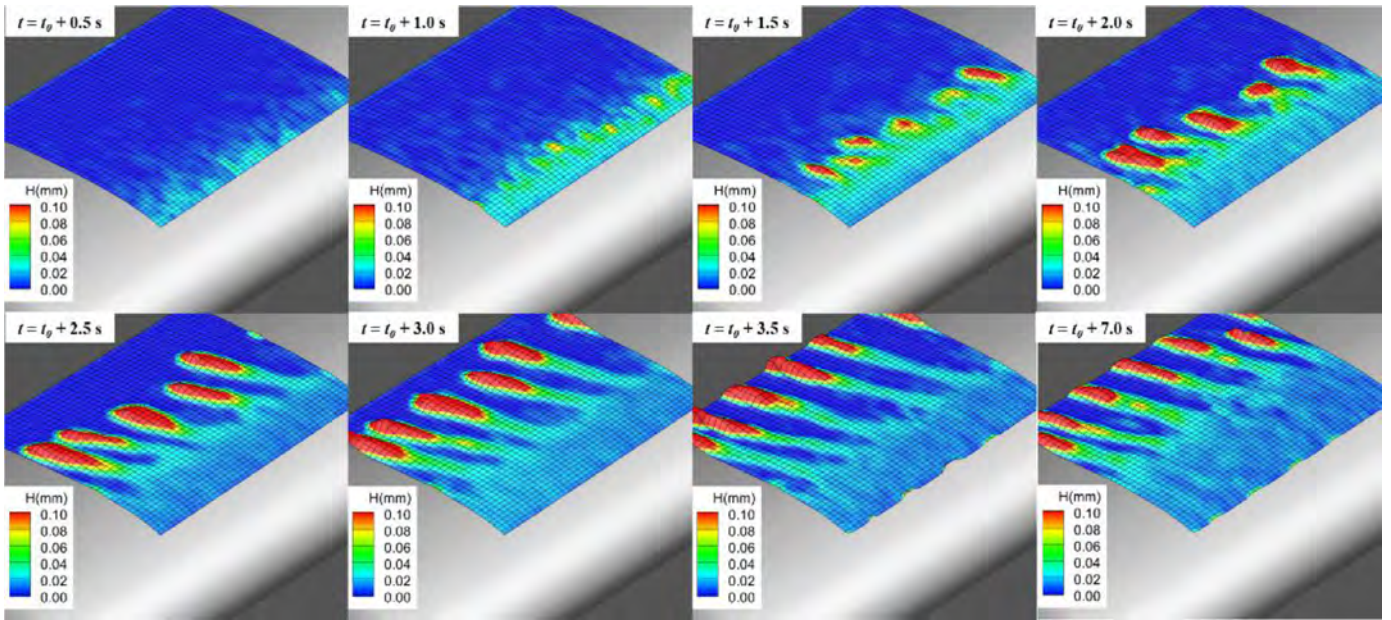
Fig. 8. Time-evolution of the surface water runback process over the airfoil model with smooth leading edge under the test condition of $U_\infty = 15$ m/s, LWC $= 5.0$ g/m^3, and $T_\infty = -5$ °C.
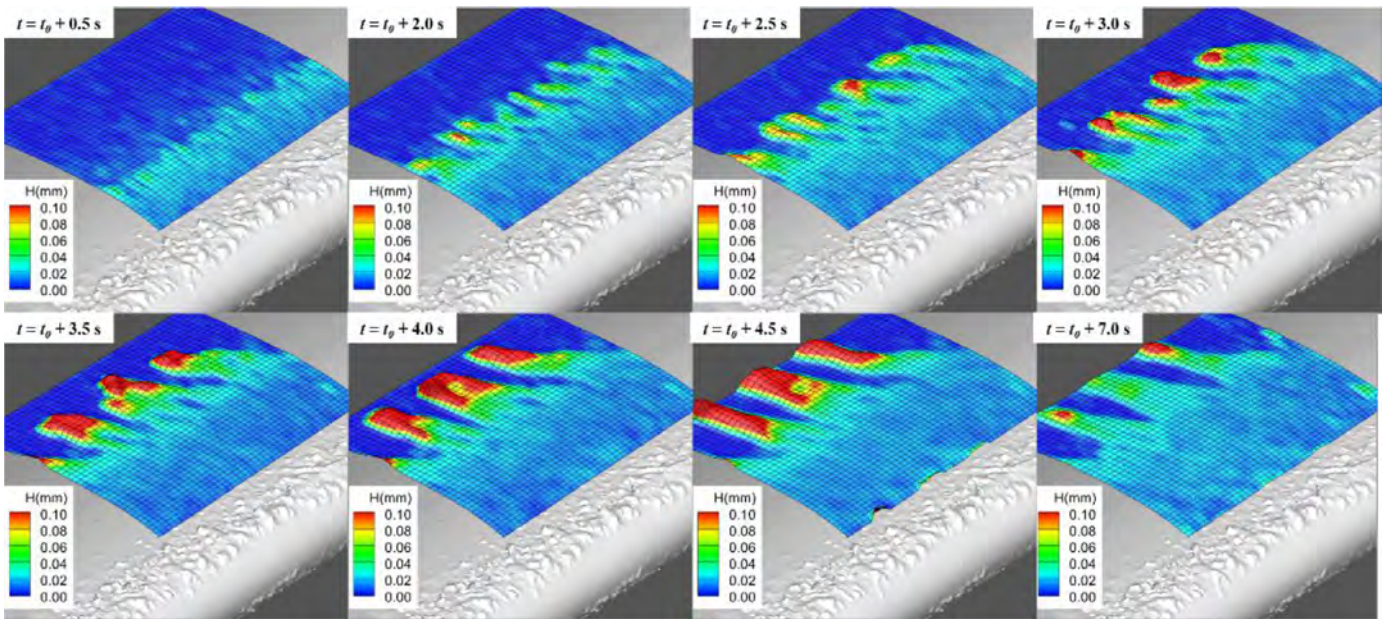

Fig. 9. Time-evolution of the surface water runback process over the airfoil model with initial leading-edge roughness under the test condition of $U_\infty = 15$ m/s, LWC $= 5.0$ g/m^3, and $T_\infty = -5$ °C.

into a water film, which then developed into evident rivulets in downstream locations as can be seen from $t = t_0 + 1.0$ to 2.5 s. During this process, the film/rivulets boundary also advanced as more water mass were collected into the surface water flow. As the rivulets moved further downstream, multiple isolated water transport channels were formed as shown in the figure ($t = t_0 + 3.0 \sim 3.5$ s). These channels became the main paths in transporting the water mass collected on the airfoil surface. It is also found that, shortly after the channel paths were formed, the wind-driven water flow became very steady as can be seen from $t = t_0 + 3.5$ to 7.0 s. In this steady state, though the water droplets were continuously collected at the airfoil leading-edge, the film/rivulets boundary only advanced slightly as can be seen in the figure.

For the surface water runback over the airfoil model with the initial leading-edge roughness (i.e., Fig. 9), it is clearly seen that, the runback water rivulets became wider, and the film/rivulets boundary developed further downstream in comparison to that over the airfoil surface with the smooth leading-edge. As the impinged water droplets coalesced and traveled through the roughness elements, the film region was found to expand further downstream as can be seen at $t = t_0 + 0.5$ s. It has been demonstrated that the roughness arrays can trap and decelerate the surface water flow (Zhang et al., 2014). Therefore, it is suggested that the realistic roughness in this study could trap and decelerate the water flow over the airfoil surface. Consequently, the inertia force in the water flow was reduced, which essentially delayed
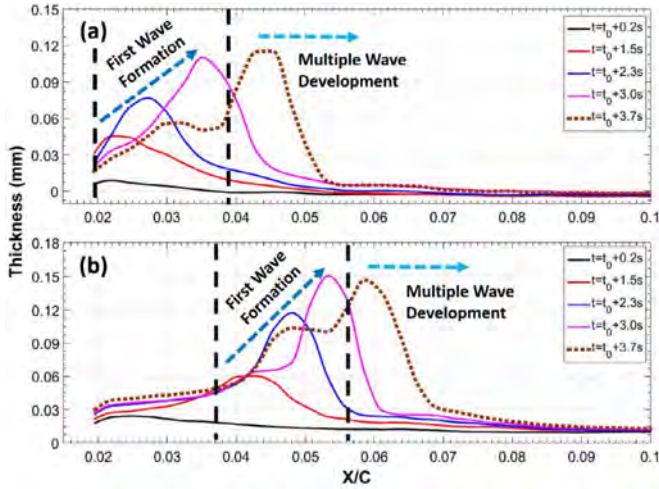
Fig. 10. Time evolution of chord-wise thickness distribution over the wing with (a) smooth and (b) rough leading edge under the test condition of $U_\infty = 10$ m/s; LWC = 5.0 g/m^3; and $T_\infty = -5$ °C.

Fig. 11. Time history of the primary wavefront locations in the water film flow over the wing with smooth (S) and rough (R) leading edge under the test condition of $U_\infty = 10$ m/s; LWC = 5.0 g/m^3; and $T_\infty = -5$ °C.

the breakup of the film front and the formation of rivulets. As time goes by, more droplets impinged on the surface, and the film broke into multiple rivulets as can be seen at $t = t_0 + 2.0$ s. It is found that, the initially formed rivulets presented evident meandering behavior. Based on the previous study, the meandering behavior is mainly caused by the non-uniformity of the advancing film front (Zhang and Hu, 2016). It has been demonstrated that realistic roughness with complex roughness topography could cause strong span-wise heterogeneities within the boundary layer flow (Barros and Christensen, 2014; Liu and Hu, 2016). Thus, the non-uniformity in the advancing film front was suggested to be initiated by the realistic roughness distribution. Due to the nature of meandering behavior, the narrow rivulets tend to merge into wider rivulets as shown from $t = t_0 + 2.5$ to 3.5 s in Fig. 9. As the rivulets merged and moved downstream, the film/rivulets boundary advanced. The initially formed rivulets were finally merged into three wide rivulets (in the measuring field) as can be seen at $t = t_0 + 4.0$ s. As more water was collected onto the airfoil surface, the rivulets act as isolated water channels that transport the water mass to further downstream ($t = t_0 + 4.0 \sim 7.0$ s).

3.2. Effects of the initial ice roughness on surface water wave formation and propagation

As mentioned above, the most evident effect of the realistic roughness on the surface water film flow is the retardation of the first wave formation. In order to further elucidate the retardation effect, we calculated the span-averaged chord-wise water film thickness distributions at different time instants for both airfoil models as shown in Fig. 10.

For the wave formation and development over the airfoil model with smooth leading-edge, the first wave started to form at 2% chord length as can be seen in Fig. 10(a). As the wave moved downstream, the wave amplitude is found to increase. It is found that, at $t = t_0 + 3.0$ s, the first wave formation was almost completed, and the wave crest was located at 3.6% chord length. According to the definition above, this first wave is called primary wave as it is the wave with the maximum amplitude. The primary wave is also known as the water film front advancing over the dry surface downstream. With the time goes by, more water was collected into the water film flow, and a secondary wave started to form as can be seen at $t = t_0 + 3.7$ s. After that, the secondary wave developed and advanced over the wetted surface before
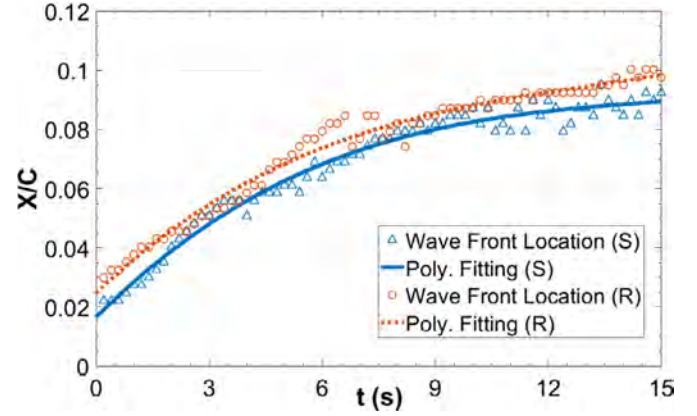
merging into the primary wave. Then, a periodical secondary wave formation and development can be observed as described in the above section. The time history of the primary wavefront locations is shown in Fig. 11. It can be seen clearly that, as the time goes by, the primary wave moved downstream with a decreasing velocity as indicated by the reducing local slope along the curve as shown in the figure. As the primary wave moved over 8% chord length, due to the solidification of the surface water mass, the wave velocity became very slow as indicated by the flattening curve in Fig. 11.

For the surface water wave formation and development over the airfoil model with the initial leading-edge roughness, i.e., Fig. 10(b), it is found that, the primary wave started to form at further downstream (3.8% chord length) in comparison to that over the airfoil model with smooth leading-edge. After a similar wave formation process, the primary wave advanced to about 5% chord length before the first secondary wave was formed. An evident retardation of the primary wave formation was observed based on the comparison in Fig. 10. It is also noticed that at $t = t_0 + 3.0$ s, the first secondary wave had started to form on the airfoil surface, which was not found in the case with the smooth leading-edge at the same time point. That means the duration of wave formation became shorter as the leading-edge roughness altered the boundary layer flow. As the primary wave moved downstream, the secondary wave formed and developed. The time history of the primary wavefront locations over the airfoil model with the initial leading-edge roughness is also plotted in Fig. 11. It can be seen clearly that, the curve for the rough leading-edge is basically parallel to the one for the smooth leading-edge, indicating that the advancing velocities of the primary waves over the two airfoil surfaces were almost the same.

3.3. Effect of the initial ice roughness on surface water rivulets formation and development

As the wind speed was increased to $U_\infty = 15$ m/s, the morphology of the surface water runback presented evident rivulet shapes over both the SLE and RLE surfaces. In the present study, a new method for recognizing the rivulets formation location and the film/rivulets boundary was proposed based on the DIP measurement results. Since the time-resolved surface water morphologies have been successfully reconstructed as shown in Figs. 6 to 9, the thickness distribution profiles of the water film/rivulets flow can be easily extracted. Then, the dry area and wetted area can be distinguished based on the water thickness distribution. For each chord-wise location, the water coverage ratio (denoted as η in this
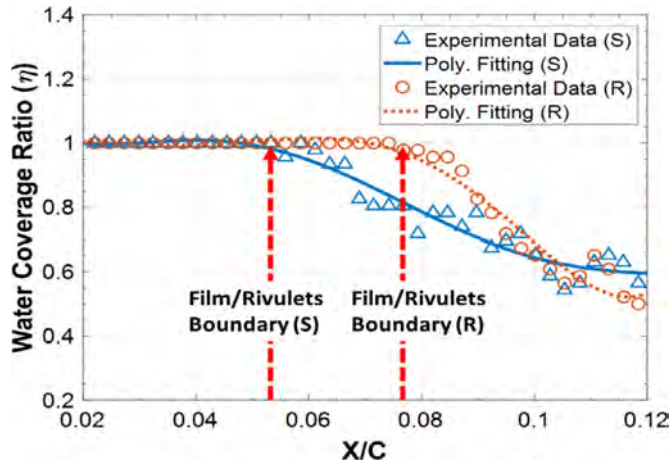
Fig. 12. Chord-wise distributions of water coverage ratio over the airfoil model with smooth and rough leading edge under the test condition of $U_\infty = 15$ m/s; LWC = 5.0 g/m³; and $T_\infty = -5$ °C.

study) can be calculated using Eq. (3).

$$\eta = \frac{wetted\ area}{total\ area} \tag{3}$$

If $\eta = 100\%$, the whole area is wetted, indicating a film morphology at the chord-wise location. Otherwise, only part of the area is wetted, and rivulets present at the location.

To illustrate the reorganization process of the rivulet formation and film/rivulets boundary, we take the instantaneous water film/rivulets morphologies at $t = t_0 + 2.8$ s for example. According to the definition, the chord-wise distribution of the water coverage ratio (η) for the water flow over the two airfoil surfaces can be derived as shown in Fig. 12. Based on the distribution curves, the film/rivulets boundaries can be easily recognized as indicated in the figure. It can be seen that the film/rivulets boundary of the water flow over the airfoil surface with SLE is located at 5% chord length while the boundary over the airfoil surface with RLE is located at 7.4% chord length. It is suggested that the water film region is extended due to the existence of the leading-edge roughness. In the rivulet region, it is also found that the water coverage ratio decreases at further downstream, indicating a transient stage of the rivulet development. As the rivulets are fully developed, the curves become flattened as can be seen in Fig. 12. The constant level of water coverage ratio is lower for the airfoil model with RLE, indicating a smaller wetted surface area.

By performing this process for each surface morphology in time series, the time evolution of the film/rivulet boundaries can be extracted as shown in Fig. 13. Based on the evolution curve for airfoil model with SLE, it is found that the rivulets start to form at 2% chord length. As time goes by, the film/rivulets boundary moves downstream with a decreasing velocity as indicated by the reducing local slope along the curve as shown in the figure. After $t = t_0 + 3.5$ s, the curve becomes flattened, and the film/rivulets boundary settles down at 5.6% chord length. As for the evolution curve for the airfoil model with RLE, it is found that the rivulets started to form at 4.2% chord length, and settles down after $t = t_0 + 3.8$ s at 8% chord length as can be seen in Fig. 13. As mentioned above, the realistic roughness could effectively trap and decelerate the water film flow, which essentially decreases the inertia force within the film front, and delays the rivulets formation. It is also found that the two evolution curves are almost parallel, indicating that the advancing velocities of the two film/rivulets boundaries are almost the same during the water runback processes.
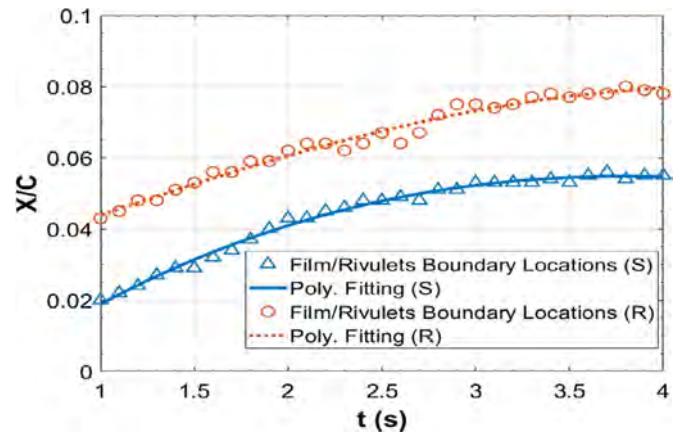

Fig. 13. Time history of water film/rivulets boundary locations over the wing with smooth and rough leading edge under the test condition of $U_\infty = 15$ m/s; LWC = 5.0 g/m³; and $T_\infty = -5$ °C.
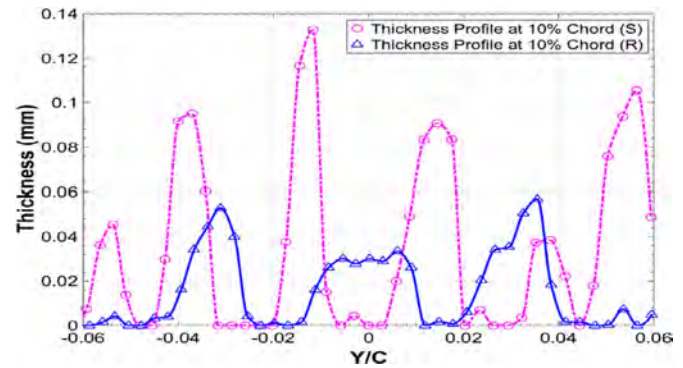

Fig. 14. Time-averaged span-wise thickness profiles in steady state at 10% chord length of the wing with smooth (S) and rough (R) leading edge under the test condition of $U_\infty = 15$ m/s; LWC = 5.0 g/m³; and $T_\infty = -5$ °C.

Based on the above analysis, it is found that as time goes by, the film/rivulets would settle down, and the rivulets flow would be in a steady state. To evaluate the rivulet shapes in the steady state, the time-averaged thickness distribution from $t = t_0 + 5.0$ to 10.0 s is also calculated in the present. Thus, the span-wise thickness profiles at downstream locations where rivulets dominate can be isolated to provide quantitative facts about the rivulet characteristics. The time-averaged span-wise thickness profiles at 10% chord length of the airfoil model with smooth (S) and rough (R) leading edge are shown in Fig. 14. Based on the rivulet center locations, the spacings between the rivulets can be estimated, and the average spacings of the rivulets on SLE and RLE are 2.2% and 3.1% chord length, respectively. It is evident that the rivulets become wider as the initial roughness forms around the leading edge as can be seen in Fig. 14. The average rivulet height is also calculated, which turns out to be 0.085 mm and 0.048 mm for SLE and RLE, respectively. It is obvious that the initial ice roughness has a significant effect on the downstream rivulet characteristics.

4. Conclusion

In the present study, an experimental study is conducted to evaluate the effects of initial ice roughness on the transient water/ice run-back process in glaze ice accretion over a NACA 23012 airfoil. The experiments were performed in the Icing Research Tunnel available at Iowa State University (ISU-IRT). A digital image projection technique was used to provide non-intrusive, temporally resolved, and full-field thickness measurements of the water/ice transport process.

The instantaneous surface morphologies of the water film/rivulets flow over the airfoil models with different leading-edge conditions (smooth and rough) were successfully reconstructed and quantified. Two typical surface water morphologies were observed: water film flow and water rivulets flow. When the wind speed is low, i.e., $U_\infty = 10$ m/s, the surface water film flow dominates, in which one primary wave and multiple secondary waves were identified as the water film moves downstream. When the wind speed increased to $U_\infty = 15$ m/s, the water film flow was found to break into multiple rivulets during the runback process. While the initial ice roughness is found to retard and shorten the primary wave formation in the water film flow, it is also found to be able to trap and decelerate the water film flow and decrease the inertia force in the film front, which essentially delays the rivulets formation. While the surface water flow is trapped by the roughness elements, it presented a meandering behavior during the rivulet formation, due to which, the initially formed rivulets merged into wider rivulets.

By recognizing the film/rivulets boundary during the dynamic water/ice runback process, the rivulets formation, transition and development were quantified. The time evolution of film/rivulets boundary was also extracted, in which the advancing velocity of the film/rivulet boundary was found to be independent of the leading-edge condition (i.e., with or without the initial ice roughness). The characteristics of the steady-state rivulets flow were also extracted. It is found that the initial ice roughness has a significant effect on the rivulet shape (e.g., rivulet width, spacing, and height).

Author contribution

Declaration of Competing Interest

The authors declare that they have no known competing financial interests or personal relationships that could have appeared to influence the work reported in this paper.

Acknowledgments

References

Appiah-Kubi, P., 2011. US Inflight Icing Accidents and Incidents, 2006 to 2010. University of Tennessee.

Barros, J.M., Christensen, K.T., 2014. Observations of turbulent secondary flows in a rough-wall boundary layer. J. Fluid Mech. 748 null-null.

Benetazzo, A., 2006. Measurements of short water waves using stereo matched image sequences. Coast. Eng. 53, 1013–1032. doi:10.1016/J.COASTALENG.2006.06.012.

Bons, J., Christensen, K., 2007. A comparison of real and simulated surface roughness characterizations. In: 37th AIAA Fluid Dynamics Conference and Exhibit, p. 3997.

Bons, J.P., 2002. St and cf augmentation for real turbine roughness with elevated freestream turbulence. In: ASME Turbo Expo 2002: Power for Land, Sea, and Air. American Society of Mechanical Engineers, pp. 349–363.

Bragg, M.B., Cummings, M.J., Lee, S., Henze, C.M., 1996. Boundary-layer and heat–transfer measurements on an airfoil with simulated ice roughness. AIAA Pap. 866, 1–16.

Cazabat, A.M., Heslot, F., Troian, S.M., Carles, P., 1990. Fingering instability of thin spreading films driven by temperature gradients. Nature 346, 824–826.

Cobelli, P.J., Maurel, A., Pagneux, V., Petitjeans, P., 2009. Global measurement of water waves by Fourier transform profilometry. Exp. Fluids 46, 1037–1047.

Du, Y., Gui, Y., Xiao, C., Yi, X., 2010. Investigation on heat transfer characteristics of aircraft icing including runback water. Int. J. Heat Mass Transf. 53, 3702–3707. doi:10.1016/j.ijheatmasstransfer.2010.04.021.

Dukhan, N., Va Jr., G., Masiulaniec, K., DeWitt, K., 1996. Convective heat transfer coefficients from various types of ice roughened surfaces in parallel and accelerating flow. AIAA, Aerospace Sciences Meeting and Exhibit.

Gendrich, C.P., Koochesfahani, M.M., 1996. A spatial correlation technique for estimating velocity fields using molecular tagging velocimetry (MTV). Experiments in Fluids 22, 67–77. doi:10.1007/BF01893307.

Gent, R.W., Dart, N.P., Cansdale, J.T., 2000. Aircraft icing. Philos. Trans. R. Soc. London. Ser. A Math. Phys. Eng. Sci. 358, 2873–2911.

Green, S.D., 2006. A study of US inflight icing accidents and incidents, 1978 to 2002. 44th AIAA Aerospace Sciences Meeting and Exhibit.

Hansman, R.J., Kirby, M.S., 1987. Comparison of wet and dry growth in artificial and flight icing conditions. J. Thermophys. Heat Transf. 1, 215–221.

Hansman, R.J., Yamaguchi, K., Berkowitz, B., Potapczuk, M., 1991. Modeling of surface roughness effects on glaze ice accretion. J. Thermophys. Heat Transf. 5, 54–60.

Henry, R., Hansman, R.J., Breuer, K.S., 1994. Measurement of heat transfer variation on surface roughness elements using infrared techniques. AIAA Pap. 94–801.

Henry, R.C., Guffond, D., Fran-atilde, G.O., Bouveret, A., 2000. Heat transfer coefficient measurement on iced airfoil in small icing wind tunnel. J. Thermophys. Heat Transf. 14, 348–354.

Henry, R.C., Hansman, R.J., Breuer, K.S., 1995. Heat transfer variation on protuberances and surface roughness elements. J. Thermophys. Heat Transf. 9, 175–180.

Hu, H., Wang, B., Zhang, K., Lohry, W., Zhang, S., 2014. Quantification of transient behavior of wind-driven surface droplet/rivulet flows using a digital fringe projection technique. J. Vis. 18, 1–14. doi:10.1007/s12650-014-0264-8.

Kerho, M., Bragg, M., 1995. Effect of large distributed leading-edge roughness on boundary layer development and transition. 13th Applied Aerodynamics Conference, Fluid Dynamics and Co-Located Conferences. American Institute of Aeronautics and Astronautics doi:10.2514/6.1995-1803.

Lee, S., Broeren, A., Addy, H., Sills, R., Pifer, E., 2012. Development of 3D ice accretion measurement method. 4th AIAA Atmospheric and Space Environments Conference, Fluid Dynamics and Co-Located Conferences. American Institute of Aeronautics and Astronautics doi:10.2514/6.2012-2938.

Lee, S., Broeren, A.P., Kreeger, R.E., Potapczuk, M.G., Utt, L., 2014. Implementation and validation of 3-D ice accretion measurement methodology. 6th AIAA Atmospheric and Space Environments Conference, AIAA Aviation. American Institute of Aeronautics and Astronautics doi:10.2514/6.2014-2613.

Liu, Y., Bond, L.J., Hu, H., 2016a. Reconstruction of wave features in wind-driven water film flow using ultrasonic pulse-echo technique. In: AIP Conference Proceedings 1706. AIP Publishing LLC doi:10.1063/1.4940461.

Liu, Y., Chen, W.-L., Bond, L.J., Hu, H., 2017. An experimental study on the characteristics of wind-driven surface water film flows by using a multi-transducer ultrasonic pulse-echo technique. Phys. Fluids 29, 012102. doi:10.1063/1.4973398.

Liu, Y., Hu, H., 2018. An experimental investigation on the unsteady heat transfer process over an ice accreting airfoil surface. Int. J. Heat Mass Transf. 122, 707–718. doi:10.1016/j.ijheatmasstransfer.2018.02.023.

Liu, Y., Hu, H., 2016. An experimental investigation on the convective heat transfer process over an ice roughened airfoil. 54th AIAA Aerospace Sciences Meeting, AIAA SciTech. American Institute of Aeronautics and Astronautics doi:10.2514/6.2016-1978.

Liu, Y., Zhang, K., Hu, H., 2016b. An experimental investigation on the water runback process over an airfoil surface with realistic ice roughness. 8th AIAA Atmospheric and Space Environments Conference. American Institute of Aeronautics and Astronautics doi:10.2514/6.2016-3140.

Liu, Y., Zhang, K., Tian, W., Hu, H., 2020. An experimental investigation on the dynamic ice accretion and unsteady heat transfer over an airfoil surface with embedded initial ice roughness. Int. J. Heat Mass Transf. 146. doi:10.1016/j.ijheatmasstransfer.2019.118900.

Mart, S.R., McClain, S.T., Wright, L.M., 2012. Turbulent convection from deterministic roughness distributions with varying thermal conductivities. J. Turbomach 134, 51030.

McClain, S.T., Kreeger, R.E., 2013. Assessment of ice shape roughness using a self-organizing map approach. 5th AIAA Atmospheric and Space Environments Conference. American Institute of Aeronautics and Astronautics, Reston, Virginia doi:10.2514/6.2013-2546.

McClain, S.T., Vargas, M., Tsao, J.-.C., Broeren, A.P., Lee, S., 2017. Ice Accretion Roughness Measurements and Modeling.

Petty, K.R., Floyd, C.D.J., 2004. A statistical review of aviation airframe icing accidents in the US. In: Proceedings of the 11th Conference on Aviation, Range, and Aerospace Hyannis.

Potapczuk, M.G., 2013. Aircraft icing research at NASA Glenn Research Center. J. Aerosp. Eng. 26, 260–276.

Rothmayer, A., 2003. On the creation of ice surface roughness by interfacial instabilities. 41st Aerospace Sciences Meeting and Exhibit, Aerospace Sciences Meetings. American Institute of Aeronautics and Astronautics doi:10.2514/6.2003-972.

Shin, J., 1996. Characteristics of surface roughness associated with leading-edge ice accretion. J. Aircr. 33, 316–321. doi:10.2514/3.46940.

Tecson, L., McClain, S.T., 2013a. Convective enhancement of surfaces with realistic ice roughness distributions. 5th AIAA Atmospheric and Space Environments Conference, Fluid Dynamics and Co-Located Conferences. American Institute of Aeronautics and Astronautics doi:10.2514/6.2013-3060.

Tecson, L., McClain, S.T., 2013b. Modeling of realistic ice roughness element distributions to characterize convective heat transfer. 5th AIAA Atmospheric and Space

Environments Conference, Fluid Dynamics and Co-Located Conferences. American Institute of Aeronautics and Astronautics doi:10.2514/6.2013-3059.

Vargas, M., 2007. Current experimental basis for modeling ice accretions on swept wings. J. Aircr. 44, 274–290. doi:10.2514/1.23323.

Waldman, R.M., Hu, H., 2015. High-Speed imaging to quantify transient ice accretion process over an airfoil. J. Aircr. 53, 369–377. doi:10.2514/1.C033367.

Winkler, J., Bragg, M., 1996. Local flowfield about large distributed roughness in the initial ice accretion process. 34th Aerospace Sciences Meeting and Exhibit, Aerospace Sciences Meetings. American Institute of Aeronautics and Astronautics doi:10.2514/6.1996-868.

Yamaguchi, K., Hansman, R.J., 1992. Heat transfer on accreting ice surfaces. J. Aircr. 29, 108–113.

Zhang, K., Hu, H., 2016. An experimental study on the transient behavior of wind-driven water runback over a flat surface. 54th AIAA Aerospace Sciences Meeting,

AIAA SciTech. American Institute of Aeronautics and Astronautics doi:10.2514/6.2016-1123.

Zhang, K., Liu, Y., Rothmayer, A.P., Hu, H., 2014a. An experimental study of wind-driven water film flows over roughness array. 6th AIAA Atmospheric and Space Environments Conference, AIAA Aviation. American Institute of Aeronautics and Astronautics doi:10.2514/6.2014-2326.

Zhang, K., Wei, T., Hu, H., 2015. An experimental investigation on the surface water transport process over an airfoil by using a digital image projection technique. Exp. Fluids 56, 1–16. doi:10.1007/s00348-015-2046-z.

Zhang, Q.-.C., Su, X.-.Y., 2002. An optical measurement of vortex shape at a free surface. Opt. Laser Technol. 34, 107–113.

Zhang, Y., Sarkar, P., Hu, H., 2014b. An experimental study on wind loads acting on a high-rise building model induced by microburst-like winds. J. Fluids Struct. 50. doi:10.1016/j.jfluidstructs.2014.07.010.